Aerostatic Stability and Bifurcation for Long-Span Bridges Based on Reduced Order Modeling via Singular Value Decomposition

Wei Cui, A.M.ASCE[1]; Junfeng Tan, S.M.ASCE[2]; Lin Zhao[3]; and Yaojun Ge[4]

Abstract: The traditional nonlinear aerostatic instability of long-span bridges is based on a two-layer iteration method that accurately predicts the structural equilibrium path before the critical buckling point. Due to strong nonlinearity after buckling, this traditional method cannot easily calculate the structural equilibrium and possible bifurcation using either Newton–Raphson or arc-length methods. In this study, a reduced order modeling (ROM) method for long-span bridge aerostatic deformation is proposed to approximate the bridge aerostatic equilibrium path after the critical point. The structural deformation mode shapes are extracted through singular value decomposition performed on the deformation matrix, and the nonlinear structural stiffness matrix is determined through the indirect displacement-based method on the finite-element method (FEM) platform. The ROM method is validated through comparison against the aerostatic deformation by the traditional two-layer iteration method based on FEM. By extending to higher wind speed, the ROM method can approximate the bridge deformation after initial buckling, and pitchfork bifurcation is observed after the structure undergoes rapid deformation growth. The stability of the equilibrium paths is examined through the Jacobian of restoring force vector, and the "snap-through" phenomenon exists for the equilibrium path before the bifurcation point. **DOI: 10.1061/JBENF2.BEENG-6427.** © *2024 American Society of Civil Engineers.*

Author keywords: Long-span bridge; Aerostatic stability; Bifurcation; Snap-through; Reduced order modeling; Singular value decomposition.

Introduction

For flexible long-span bridges, there are two typical aerodynamic instabilities: aeroelastic flutter and aerostatic instability (Yang et al. 2015). Flutter occurs when a periodically moving body in a fluid flow exhibits negative damping caused by positive feedback between bridge deck displacement and motion-dependent

[1]Assistant Professor, State Key Lab of Disaster Reduction in Civil Engineering, Tongji Univ., Shanghai 200092, China; Key Laboratory of Transport Industry of Wind Resistant Technology for Bridge Structures, Tongji Univ., Shanghai 200092, China; Dept. of Bridge Engineering, College of Civil Engineering, Tongji Univ., Shanghai 200092, China (corresponding author). ORCID: https://orcid.org/0000-0001-7489-923X. Email: cuiwei@tongji.edu.cn

[2]Graduate Student, State Key Lab of Disaster Reduction in Civil Engineering, Tongji Univ., Shanghai 200092, China; College of Civil Engineering, Chongqing Jiaotong Univ., Chongqing 400074, China. ORCID: https://orcid.org/0009-0005-7805-5866. Email: tanjunfeng@mails.cqjtu.edu.cn

[3]Professor, State Key Lab of Disaster Reduction in Civil Engineering, Tongji Univ., Shanghai 200092, China; Key Laboratory of Transport Industry of Wind Resistant Technology for Bridge Structures, Tongji Univ., Shanghai 200092, China; Dept. of Bridge Engineering, College of Civil Engineering, Tongji Univ., Shanghai 200092, China. Email: zhaolin@tongji.edu.cn

[4]Professor, State Key Lab of Disaster Reduction in Civil Engineering, Tongji Univ., Shanghai 200092, China; Key Laboratory of Transport Industry of Wind Resistant Technology for Bridge Structures, Tongji Univ., Shanghai 200092, China; Dept. of Bridge Engineering, College of Civil Engineering, Tongji Univ., Shanghai 200092, China. Email: yaojunge@tongji.edu.cn

aeroelastic force. Aerostatic instability, also known as torsional divergence in aeronautical engineering, is caused by fast-growing aerostatic loads and softening stiffness due to geometry nonlinearity. On one side, the aerodynamic pitch moment increases the wind flow angle of attack (AoA) on the bridge deck, which further increases the aerodynamic forces, and, on the other side, the deck torsion deforms the cable–hanger–deck system and then decreases the structural stiffness due to geometry nonlinearity. In the beginning, aerostatic stability is also known as the torsional divergence of flight wings in the aeronautical engineering field, which was defined by a critical wind speed at which the torsion caused negative aerodynamic stiffness to surpass structural stiffness, and structural torsion will increase unlimitedly (Bisplinghoff and Ashley 2013). Initially, the critical wind speed can be calculated assuming that both pitch moment and structural restoring force vary linearly with torsional deformation. For long-span bridges, based on the same linearity assumption, the critical wind speeds can be derived from structural stiffness and aerodynamic pitch moment coefficients (Simiu and Yeo 2019). In the wind tunnel test of a full-bridge model of long-span bridges, flutter usually occurs before aerostatic torsional divergence (Simiu and Scanlan 1996), but for some particular bridges, torsional divergence occurred earlier than flutter instability under static wind loads (Hirai et al. 1967).

However, the linearity assumption is normally unsuitable for long-span suspension or cable-stayed bridges because of geometry nonlinearity, aerodynamic nonlinearity, and even material strength nonlinearity. Therefore, the finite-element method (FEM) was employed to investigate the wind-induced nonlinear lateral-torsional buckling of cable-stayed bridges through combining eigenvalue analysis and updated bound algorithms (Boonyapinyo et al. 1994). Later, the material strength nonlinearity was also considered in the lateral-torsional buckling analysis for suspension bridges (Boonyapinyo et al. 2006). At the same time, a two-layer nested iteration method was developed based on nonlinear FEM to analyze

the aerostatic stability for a suspension bridge (Cheng et al. 2002). In addition to torsional divergence, it was also found out that the vanishing of pretension is another criterion for long-span bridge lateral-torsion buckling (Zhang et al. 2015).

In addition to numerical simulation methods, the analytical method is also another important tool for static wind loads induced instability. Classical analyses of torsional divergence, based on the linear assumption of aerodynamic force and structural stiffness, can be solved by a Sturm–Liouville eigenvalue problem (Bisplinghoff and Ashley 2013). Other analytical methods considering geometrical and aerodynamic nonlinearity have also been developed for general prim beam (Dimentberg 1999) and flight wings (Dunn and Dugundji 1992) in the field of aeronautical engineering. The long-span bridge has a more complex structural system composed of a bridge girder, cable system, and bridge tower. Therefore, it is more difficult to derive an analytical framework for lateral-torsional buckling analysis. Based on a certain simplification, a nonlinear model of torsional divergence and flutter for suspension bridges was parameterized based on a single generalized coordinate (Arena and Lacarbonara 2012). The asymmetric wind field effect on the static torsional divergence of flexible suspension bridges was also studied, which reveals that the structural stability is worse under asymmetric wind loading (Zhang and Zhu 2021). Recently, a pseudo-three-dimensional (3D) method based on the finite-volume solution and element-free Galerkin methods has been developed for the aerostatic instability of long-span bridges (Zamiri and Sabbagh-Yazdi 2021). In the meantime, a novel aerostatic stability analysis method based on the dynamic model decomposition was proposed by Montoya et al. (2021), which found that the structural collapse is driven by the stiffness degradation. The feasibility study of a two-stage geometric nonlinear analysis method has been discussed (Tsay 2021). The effect of aerostatic instability for the long-span bridges with different span has been investigated (Hu et al. 2019), and a possible aerodynamic countermeasure to reduce the aerostatic wind loads has been simulated and verified through wind tunnel tests (An et al. 2022). Nevertheless, when multisources nonlinearity is included in the lateral-torsional buckling, FEM is still the most convenient tool for a complex structural system, such as long-span bridges.

However, several analytic methods have been proposed about the aeroelastic responses considering both structural and aerodynamic nonlinearity. Ebrahimnejad et al. (2014) used an eigensystem realization algorithm to establish a reduced order model, which can efficiently simulate the unsteady aerodynamic force subjected to arbitrary motion. The nonlinear postcritical aeroelastic vibration was investigated by the parametric modeling by Arena et al. (2016). Abbas et al. (2020) developed an artificial neural network to predict the bridge aeroelastic response. In summary, there are already several widely used aeroelastic models to simulate the dynamic response of long-span bridges.

As the bridges span increases continuously in engineering practice, it is noticed that the geometry and aerodynamic nonlinearity become more remarkable than current constructed long-span bridges (Ge et al. 2018). The critical aerostatic wind speeds reduced greatly as the span increased. Table 1 (Ding et al. 2023) lists five selected super long-span suspension bridges and associated aerostatic critical wind speeds. It clearly reveals that bridge resistance capacity against static wind loads decreases rapidly when the bridge span increases. Therefore, it is necessary to explore the structural behavior after the initial buckling at the first critical wind speeds. Because of the geometry and aerodynamic nonlinearity, it is possible that the equilibrium path will have a "snap-through" phenomenon or even bifurcation (multiple stability) occurs. However, existing methods based on FEM are unable to track multiple equilibrium paths when bifurcation occurs. The major nonlinear solver in the current FEM platform is the Newton–Raphson method, which cannot track the equilibrium path that surpasses the first critical point. The arc-length method, another popular nonlinear solver, can track the equilibrium path through a singular point till the final divergence. However, it is difficult to track multiple equilibrium paths after the bifurcation point.

The bifurcation phenomenon for torsional-divergence under static wind loads was investigated for aircraft wings (Fazelzadeh and Mazidi 2011). The nonlinear structural formulation for wings is based on the von Kármán large deformation theory. For complex structures such as long-span suspension bridges, it is difficult to derive the nonlinear structural formulation analytically. Overall, it is necessary to develop a new method to study the bridge nonlinear aerostatic problem with the bifurcation phenomenon.

This paper proposes a reduced order method for bridge aerostatic stability based on orthogonal modes decomposition. The modes decomposition employed in this paper does not rely on traditional dynamic modes decomposition, and a new modes decomposition based on singular value decomposition (SVD) is proposed. At first, the standard aerostatic stability analysis is performed at three different AoA ($-3°$, $0°$, $3°$). Next, the bridge girder deflection modes are derived based on SVD of the matrix composed by the bridge girder deformation shapes under various wind speeds and AoA. The nonlinear structural formulas for the reduced order model are calibrated by the displacement indirect/nonintrusive method (Mignolet et al. 2013). Consequently, the governing equation of structural deflections under aerostatic loads is established, and the multiple equilibrium paths after the bifurcation point are solved by a simple nonlinear equations solver. Since the number of degrees of freedom is greatly reduced, the computation cost is also considerably decreased, and the strong nonlinearity after large deformation can also be solved approximately for these reduced order models. At the postbuckling stage with large deformation, the reduced order modeling (ROM) method can still roughly estimate the structural deformation efficiently with a little lower accuracy. In contrast, FEMs normally cannot be converged because of the large number of degrees of freedom.

Reduced Order Modeling of Long-Span Bridge Aerostatic Deformation

Aerostatic Equilibrium Mechanism

Fig. 1 illustrates the bridge section external force and motion per unit span. The wind loads per unit span applied on the bridge

Table 1. Typical long-span suspension bridges' main span versus critical aerostatic wind speeds

Bridge name	Span length (m)	Aerostatic critical wind speed (m/s)
Xihoumen Bridge	1,650	95
Lingding Bridge	1,666	99.2
Nansha Bridge	1,688	82
Lianhuashan Bridge	2,100	87.5
Shiziyang Bridge	2,180	85

section can be decomposed into three components along the wind axis: drag force F_D, lift force F_L, and pitch moment F_M,

$$F_D = \frac{1}{2}\rho U^2 B C_D(\alpha) \tag{1a}$$

$$F_L = \frac{1}{2}\rho U^2 B C_L(\alpha) \tag{1b}$$

$$F_M = \frac{1}{2}\rho U^2 B^2 C_M(\alpha) \tag{1c}$$

where U is the mean wind speed inclined with initial AoA α_0, ρ is the air density, and B and D are bridge deck width and depth, respectively. The long-span bridge displacements along span are expressed along bridge global coordinates: sway $p(x)$ (horizontal), hover $h(x)$ (vertical), and pitch $\theta(x)$ (torsional). Here, $C_D(\alpha)$, $C_L(\alpha)$, and $C_M(\alpha)$ are drag, lift, and pitch coefficients, respectively, at effective AoA $\alpha = \alpha_0 + \theta$.

The three directional wind loads defined in Eq. (1) are along the wind axis, which should be converted to the global axis in FEM. The relation between forces vector in wind axis and in global axis is defined as

$$\begin{Bmatrix} F_D \\ F_L \\ F_M \end{Bmatrix} = \begin{bmatrix} \cos(\alpha_0) & \sin(\alpha_0) & 0 \\ -\sin(\alpha_0) & \cos(\alpha_0) & 0 \\ 0 & 0 & 1 \end{bmatrix} \begin{Bmatrix} F_X \\ F_Y \\ F_M \end{Bmatrix} \tag{2}$$

The nonlinear equilibrium equations under static wind loads is

$$K(d)d = F(U, d) \tag{3}$$

in which d is the 3D bridge deck deflection along span coordinate x including three components: sway $p(x)$, hover $h(x)$, and pitch $\theta(x)$, and thus $d = [p(x) \; h(x) \; \theta(x)]^T$; $K(d)$ is the nonlinear stiffness matrix depending on d, and $F(U, d)$ are the nonlinear wind loads matrix depending on wind speeds U and d as well.

For the long-span bridge, aerostatic stability analysis, gravity loads, including dead loads and cable pretension, are normally applied at first to initialize the gravitational stiffness.

Bridge Aerostatic Deflection Model and Reduced Order Modeling

According to the commercial FEM software, the deflection of a bridge girder affected by increasing wind speeds can be calculated by a two nested loops algorithm (Cheng et al. 2002). The outer loop is iterating wind speeds, and the inner loop is calculating structural deflection to achieve the balance of deflection-dependent wind loads and structural restoring forces.
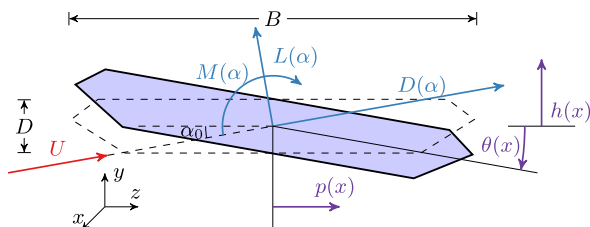

Fig. 1. Wind loads axis and bridge motion axis on bridge section.

Here, d is expanded as a summation of orthogonal deflection modes ϕ_r and associated generalized coordinates q_i:

$$d = \sum_{i=1}^{L} \phi_i q_i = \Phi q \tag{4}$$

where L is the expansion order and i is the looping index.

Then the equilibrium equation is rewritten as

$$\hat{K}(d)q = \hat{F}(U, d) \tag{5}$$

where $\hat{K} = \Phi^T K \Phi$ with dimension as $L \times L$ and $\hat{F} = \Phi^T F$ with dimension as $1 \times L$, and $\hat{K}(d)$ is the nonlinear generalized stiffness matrix to be identified. Normally, L is much less than the degrees of freedom of original equilibrium equations in Eq. (3) and, thus, Eq. (5) is called the reduced order model.

The methods to determine parameters in $\hat{K}(d)$ include the direct method (Przekop et al. 2004), displacement-based indirect method (Muravyov and Rizzi 2003), and force-based indirect method (Hollkamp et al. 2005). A detailed literature review about ROM of nonlinear structures is provided by Mignolet et al. (2013). The displacement-based method is employed in this study and the procedure is described in the following.

Determination of Nonlinear Stiffness Parameters

In the reduced order equilibrium equation of Eq. (5), the ith component can be expressed explicitly in Einstein summation notation as

$$\hat{F}_i = \hat{K}_{ij}^{(1)} q_j + \hat{K}_{ijl}^{(2)} q_j q_l + \hat{K}_{ijlp}^{(3)} q_j q_l q_p, \quad i, j, l, p = 1, \ldots, L \tag{6}$$

in which $\hat{K}_{ij}^{(1)}$, $\hat{K}_{ijl}^{(2)}$, and $\hat{K}_{ijlp}^{(3)}$ are linear, quadratic, and cubic stiffness terms in generalized coordinates. The nonlinear structural stiffness comes from geometry nonlinearity of a suspension bridge. The detailed process for $L = 2$ has been demonstrated by Muravyov and Rizzi (2003), and will be summarized briefly here.

First, for stiffness terms with the same lower indices as $\hat{K}_{ij}^{(1)}$, $\hat{K}_{ijj}^{(2)}$, and $\hat{K}_{ijjj}^{(3)}$, three prescribed displacements d in Cartesian coordinates are applied on the finite-element model

$$d^{[1]} = q_j \phi_j \quad d^{[2]} = -q_j \phi_j \quad d^{[3]} = \bar{q}_j \phi_j \tag{7}$$

where q_j and $\bar{q}_j$ are two different scalar numbers in the jth generalized coordinate.

Correspondingly, the generalized restoring forces in the ith generalized coordinate due to prescribed displacements can be determined through commercial FEM software:

$$\begin{aligned} \hat{F}_i^{[1]} &= \hat{K}_{ij}^{(1)} q_j + \hat{K}_{ijj}^{(2)} q_j^2 + \hat{K}_{ijjj}^{(3)} q_j^3 \\ \hat{F}_i^{[2]} &= -\hat{K}_{ij}^{(1)} q_j + \hat{K}_{ijj}^{(2)} q_j^2 - \hat{K}_{ijjj}^{(3)} q_j^3 \\ \hat{F}_i^{[3]} &= \hat{K}_{ij}^{(1)} \bar{q}_j + \hat{K}_{ijj}^{(2)} \bar{q}_j^2 + \hat{K}_{ijjj}^{(3)} \bar{q}_j^3 \end{aligned} \tag{8}$$

For the stiffness terms with different lower indices as $\hat{K}_{ijl}^{(2)}$, $\hat{K}_{ijjl}^{(3)}$, and $\hat{K}_{ijll}^{(3)}$, the prescribed displacements d are changed as

$$d^{[1]} = q_j \phi_j + q_l \phi_l \quad d^{[2]} = -q_j \phi_j - q_l \phi_l \quad d^{[3]} = q_j \phi_j - q_l \phi_l \tag{9}$$

It should be noted that, because of stiffness matrix symmetricity, $\hat{K}_{ijl}^{(2)} = \hat{K}_{ilj}^{(2)}$ and $\hat{K}_{ijjl}^{(3)} = \hat{K}_{ijlj}^{(3)}$. Then $\hat{K}_{ijl}^{(2)}$, $\hat{K}_{ijjl}^{(3)}$ and $\hat{K}_{ijll}^{(3)}$ can be determined in an analogous way as in Eq. (8).
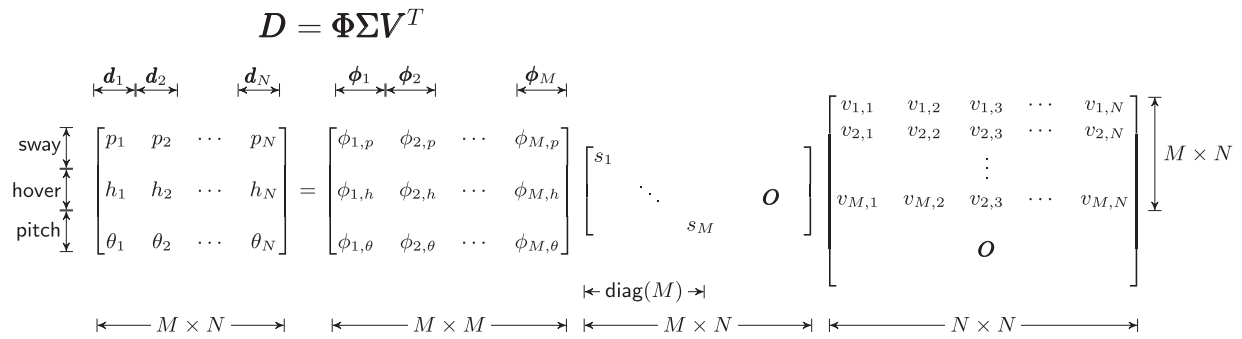
$$D = \Phi \Sigma V^T$$

Fig. 2. Illustration of SVD of deformation matrix $\boldsymbol{D}$.

Deformation Mode Derived by Singular Value Decomposition

Before determining the coefficients in Eq. (6), the mode shape in reduced order mode should be derived first. The most widely used mode decomposition is the dynamic mode derived from generalized eigenvalue decomposition of the structural stiffness matrix $\boldsymbol{K}$ to mass matrix $\boldsymbol{M}$ (Clough and Penzien 1975). It is tempting to directly use the dynamic mode because these mode shapes can be employed for both aerostatic and aerodynamic problems. Montoya et al. (2021) has proved that the reduced order method based on dynamic model decomposition is able to simulate the aerostatic instability. However, because of the continuity and uniformity of long-span bridges, each dynamic mode has only one single deformation: sway, hover, or pitch. Therefore, the minimum expansion order L is six if at least one higher-order mode is necessary ($L = 3 \times 2 = 6$). Sequentially, the number of coefficients for nonlinear stiffness terms will be considerably large ($6^2 + 6^3 + 6^4 = 1{,}548$), which makes the determination of the reduced order model impractical. As a result, it is necessary to develop an alternative mode decomposition method, including deformation along with multiple directions in each mode. It should be noted that the mode decomposition method proposed in this study is only suitable for the aerostatic analysis. If the structural dynamics and aeroelasticity are considered, the ROM should be performed on the traditional dynamic mode decomposition.

The FEMs introduced in the previous section can calculate the bridge girder's deformation $\boldsymbol{d}$ under aerostatic loads at various wind speeds U and initial AoA α_0. A sequence of deformation $\boldsymbol{d}_i$ for a combination of $(U_i, \alpha_{0,i})$ compose a deformation matrix $\boldsymbol{D} = [\boldsymbol{d}_1 \quad \boldsymbol{d}_2 \quad \cdots \quad \boldsymbol{d}_N]$, where $\boldsymbol{d}_i$ can be considered as a "snapshot" (Muller et al. 2004) of long-span bridge aerostatic deformation and N is the total number of snapshots.

In the next step, the deformation mode can be derived by SVD (Klema and Laub 1980) expressed by

$$\boldsymbol{D} = \boldsymbol{\Phi} \boldsymbol{\Sigma} \boldsymbol{V}^T \tag{10}$$

where $\boldsymbol{\Phi}$ is the mode shape matrix, and $\boldsymbol{\Sigma}$ is a diagonal matrix composed by singular values (mode significance) and mode participation matrix $\boldsymbol{V}$. SVD has been widely used in the field of computer vision, such as digital recognition (Bergqvist and Larsson 2010), face recognition (Asiedu et al. 2014), and image compression (Rufai et al. 2014). Recently, SVD has become an emerging technology for aerodynamic modeling (Lorente et al. 2008) and building pressure modeling (Tamura et al. 1997; Kim and Tse 2018).

The components of SVD are illustrated in Fig. 2. Each $\boldsymbol{d}_i$ is composed by the deformation in the sway p_i, hover h_i, and pitch θ_i directions. The number of nodes on the bridge girder is denoted as m. Thus, the total number of degrees of freedom is $M = 3 \times m$.

Correspondingly, each mode shape array $\boldsymbol{\phi}_i$ also composes the mode shape in the sway $\phi_{i,p}$, hover $\phi_{i,h}$, and pitch $\phi_{i,\theta}$ directions. Normally, the number of "snapshots" N is greater than M, and, therefore, matrices $\boldsymbol{\Sigma}$ and $\boldsymbol{V}$ are both right padded with zeros to keep the matrix size consistent ($\boldsymbol{V}^T$ is bottom padded as depicted in Fig. 2).

By the characteristic of SVD, the mode significance expressed by singular values s_i in matrix $\boldsymbol{\Sigma}$ drops exponentially (Benjamin Erichson et al. 2017). Therefore, it is possible to compress the deformation matrix $\boldsymbol{D}$ through a much smaller mode number $L << M$, and so that

$$\boldsymbol{D} \approx \hat{\boldsymbol{\Phi}} \hat{\boldsymbol{\Sigma}} \hat{\boldsymbol{V}}^T \tag{11}$$

where $\hat{\boldsymbol{\Phi}}$, $\hat{\boldsymbol{\Sigma}}$, and $\hat{\boldsymbol{V}}$ are the corresponding reduced order matrices with modes number as L. The reduced order SVD is illustrated in Fig. 3. Here, $\hat{\boldsymbol{\Phi}}$ is the left first L modes extracted from $\boldsymbol{\Phi}$, $\hat{\boldsymbol{\Sigma}}$ is the a diagonal matrix composed by $\hat{\boldsymbol{\Sigma}} = \text{diag}[s_1 \quad \cdots \quad s_L]$, and $\hat{\boldsymbol{V}}$ is the left first L columns extracted from $\boldsymbol{V}$ ($\hat{\boldsymbol{V}}^T$ is the top first L rows).

Bifurcation Theory in Nonlinear System

A bifurcation occurs when a small smooth change made to the parameter values (the bifurcation parameters) of a system causes a sudden "qualitative" or topological change in its behavior (Kielhöfer 2011). Among several types of bifurcation, pitchfork bifurcation is a particular type of local bifurcation where the system transitions from one fixed point to three fixed points.

For the aerostatic stability of long-span bridges, the possible bifurcation after the first critical points has rarely been investigated. Traditionally, in a small range of AoA, the aerostatic force coefficients are nearly linear and geometry nonlinearity is also not obvious for the bridge with a relatively short span. However, several newly constructed bridges reach a span over 2,000 m, such as Shiziyang Bridge and Çanakkale 1915 Bridge, and proposed bridges even reach 3,000 m (Messina Bridge) and 5,000 m (Taiwan strait Bridge Ge et al. 2018). Because of the more challenging aerodynamic stability, the bridge cross-section shape is more complex, as the Messina Bridge adopted a double-slotted section. As a result, the aerostatic force coefficients may vary nonuniformly as the AoA increases. Therefore, it is possible that the nonlinear behavior of long-span bridges under aerostatic loads may become more complex, and bifurcation points may exist at large wind speeds. As the traditional methods (linear equation and FEM) are unable to solve the bifurcation problem, it is necessary to develop a new method to analyze the bifurcation behavior (multiple stable states) of aerostatic stability for long-span bridges.

© ASCE

04024076-4

J. Bridge Eng.

$$D \approx \hat{\Phi}\hat{\Sigma}\hat{V}^T$$

Fig. 3. Illustration of reduced order SVD of deformation matrix D.
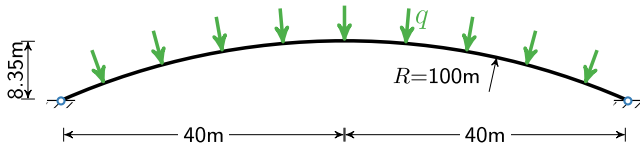
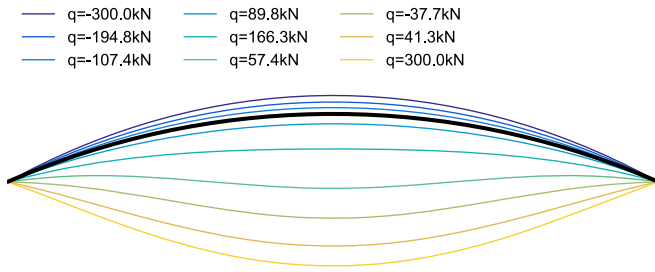**Fig. 4.** Geometry of arch beam under uniform distributed loads.

Fig. 5. Beam's deflection shape for $q = -300 \sim 300$ kN from FEM results.

Verification of ROM Method Based on SVD

Before implementing the proposed method on complex long-span bridges, a simple two-dimensional (2D) arch beam under uniform distributed loads is employed to verify this method. The geometry and boundary conditions are provided in Fig. 4. The beam width and height are 80 m and 8.3485 m, respectively, and the radius of the beam's arc is 100 m. The arc radius is $2 \times \arcsin(0.4) \approx 47.16°$. The two ends of the beam are both hinged. The uniform distributed loads are pointed to the arc center. The beam's material properties are defined as $EI = 1 \times 10^7$ kN m^2 and $EA = 3.2 \times 10^6$ kN.

The deflection shape with geometry nonlinearity for $q = -300 \sim 300$ kN are calculated through the ANSYS platform, and some deflection shapes at selected load steps are plotted in Fig. 5. Under the negative q, the arch beam is in tension and the stiffness is positive. Under positive q, the arch beam is in compression at the initial stage; however, when q exceeds the critical points, the beam deformed at large amplitude and negative stiffness is observed afterward. When q exceeds the second critical point, the beam is in tension and regains the positive stiffness. To fully examine the accuracy of the proposed ROM method, only deformation shapes before the critical point, as well as $q > 0$, are extracted to ensemble the deformation matrix in Eq. (11).

Employing the SVD algorithm introduced in the previous section, the singular values are plotted in Fig. 6. The first mode

dominates the beam deflection shape, and the value on the second mode is marginal. The values from the third mode are negligible. Therefore, the first two modes are employed for ROM. The first and second mode shapes are plotted in Fig. 7. Since the external load is symmetric, the deflection mode shapes are also symmetric. The second mode shape has three points of contraflexure, which means that more internal deformation energy is required to maintain the mode 2 shape.

The nonlinear stiffness matrix for the ROM is determined by the indirect displacement-based method, from which the beam's deflection can also be determined by a simple nonlinear equations solver. The results from ROM for various q are plotted in Fig. 8. The results comparison reveals that even though the mode shapes are extracted only from the partial deformation information when $0 < q < 166$ kN, the ROM can approximate the beam's deformation far beyond this range, including the softening range. However, in the restiffening range after middle deflection larger than 12 m, there is a clear difference between the FEM and ROM results because the two mode shapes are not enough to capture the arc-beam deformation, and an extra mode shape appears at this stage. Nevertheless, the restiffening behavior is still captured by the ROM. In summary, ROM is able to provide approximate deformation for the nonlinear structure under static loads at a very small computation cost even when the deformation is very large.

Fig. 9 displays the deformation shape of an arch beam at several key points, and Fig. 8 also plots the load–deformation relationship at those key points. Point "A" is for the arch beam in tension, and Point "B" is for the arch beam in compression with largest force. After point "B," the deformation continues to increase, but the
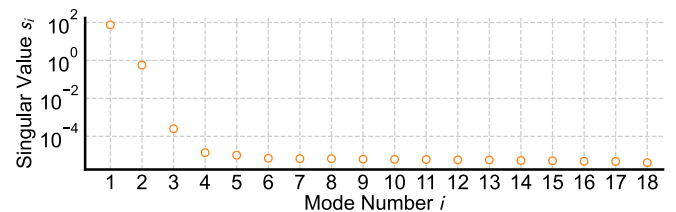

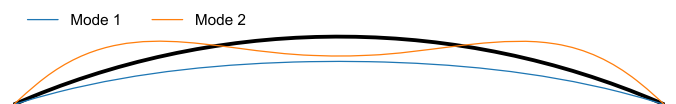**Fig. 6.** The first 18 singular values s_i calculated by SVD on D for the arch beam.

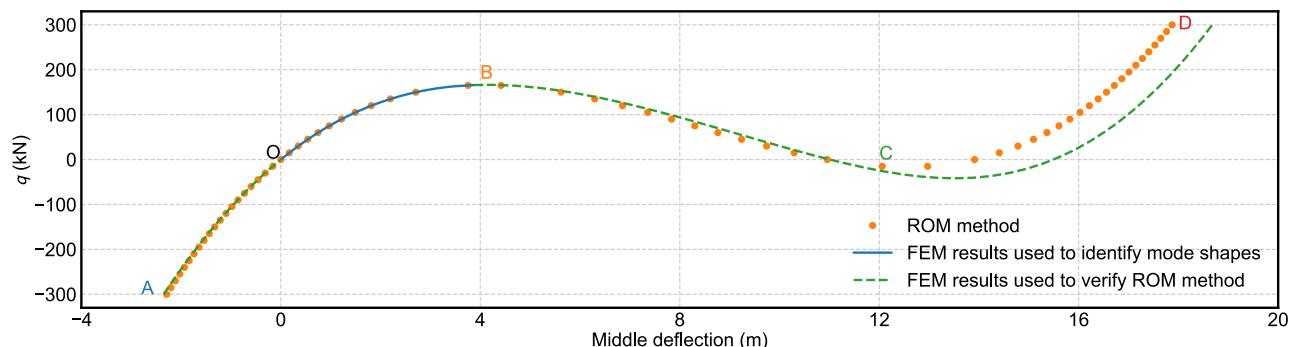**Fig. 7.** The shapes of first two modes extracted by SVD.

Fig. 8. The middle point's deformation results comparison between FEM and reduced order results.
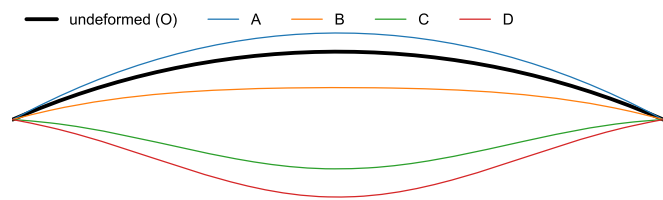

Fig. 9. The middle point's deformation results comparison between FEM and reduced order results.

force start to decrease until point "C." After point "C," the arch beam is in tension, and both the deformation and loads increase.

Application of Reduced Order Modeling for Aerostatic Stability of Long-Span Bridges with Multiple Stable States

Finite-Element Methods Modeling of Long-Span Bridge

At first, a virtual long-span bridge is constructed on a commercial FEMs software platform (ANSYS). In this study, an example long-span bridge with a main span of 3,000 m and deck width of 50 m was employed. The sketch of the bridge is illustrated in Fig. 10. To ensure the understandability of the ROM method, the suspension bridge is reduced to the most simplified form. The bridge tower is omitted, and the main cables are hinged at the top.

Tensile link (LINK180) elements are employed to model the suspended cables (curved line at the top in Fig. 10) and hangers (vertical lines at the middle in Fig. 10). The main bridge girder (horizontal line at the bottom in Fig. 10) is also mod-eled using Euler beam elements (BEAM188) and connected to hangers through a rigid "fish-bone" framework (Ko et al. 1998). The bridge girders and suspension cables are discretized at the hanger locations.

For the boundary conditions, the two ends of both bridge girder and main cables are all simply supported (three directional translational displacements are restricted). Thus, the bridge towers are

omitted. The main parameters of this virtual bridge are listed in Table 2.

A typical center-slotted twin-box sectional model is employed as the prototype bridge section in this study. The detailed geometries of the bridge section are depicted in Fig. 11. As depicted in Fig. 11, the two decks are connected through stiff beams, so the two parallel decks can be treated as a whole body.

The material nonlinearity effect on the aerostatic instability had been reported differently in previous studies. Boonyapinyo et al. (2006) stated that the critical wind speeds of a suspension bridge with truss section can be greatly reduced by the material nonlinearity. However, Shao (2010) revealed that the material nonlinearity has almost zero effect on four suspension bridges with different streamlined section. Since the bridge section in Fig. 11 is a typical streamlined section, the material nonlinearity is not considered, but geometry and aerodynamic nonlinearity are included in this study.

Based on the section shape geometries, this sectional model was tested in the wind tunnel, in Fig. 12, to measure the aerostatic coefficients. The overall sectional model width is 85 cm, the height is 8.8 cm, and the central slot width is 12.5 cm. The measured drag coefficient C_D, lift coefficient C_L, and pitch coefficient C_M for the AoA α in the range ($-12° \sim 12°$) are plotted as scatter points in Fig. 13. The C_D is nearly symmetric, while C_L and C_M are nearly asymmetric with some offset at 0°. Therefore, to smooth the aerostatic loads calculated in the latter steps, the smoothed spline (Koenker et al. 1994) is used to fit the discrete wind tunnel results. The smoothed spline interpolation and extrapolation of C_D, C_L, and C_M are also plotted in Fig. 13.

Aerostatic Deformation Calculated by FEM

According to the computation procedure mentioned above and the long-span bridge properties described in the previous section, aerostatic buckling analysis can be performed for prescribed initial wind AoA. Fig. 14 depicts the bridge aerostatic displacements at-middle span $x = L/2$ along horizontal p, vertical h, and torsional θ directions for various wind speeds U with initial AoA $\alpha_0 = -3°, 0°, 3°$. The range of initial AoA may be defined in the local wind engineering design code (Ministry of Transports of the People's Republic of China 2018). It should be noted, when
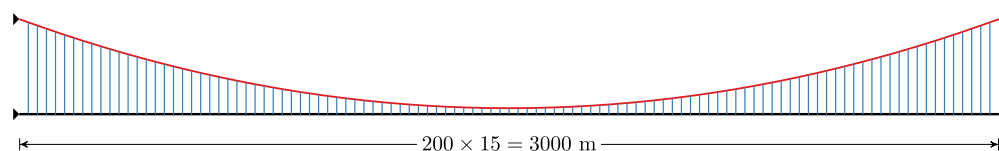

Fig. 10. FEM model of a virtual bridge.

Table 2. Consistent structural parameters of six bridge models

Parameters	Values
Main span	3,000
Sag–span ratio	1/11
Deck width B (m)	50
Deck thickness D (m)	4
Mass per unit length M (kg/m)	40,000
Mass moment of inertia along longitudinal axis per unit length I (kg·m^2/m)	4,500,000
Area of bridge section (m^2)	1.11
Area moment of inertia $I_x/I_y/I_z$ (m^4)	5.5/2.64/94
Area of main cable (m^2)	0.95
Hanger	Massless and infinite stiffness
Structural damping ratio	0.003
Air density ρ (kg/m^3)	1.25

a wider range of initial AoA is required, more modes should be included in the ROM of long-span bridges. The displacement curves reveal that aerostatic buckling for $\alpha_0 = 3°$ is a typical limit-point buckling (Leahu-Aluas and Abed-Meraim 2011). When wind speed $U \geq 46$ m/s, the structural deformation at all three directions grows dramatically, and the FEM model cannot converge to a stable equilibrium point. However, for the other two vertical and torsional directions, the traditional method cannot find the typical limit-point. Because of the two-layer loop algorithm, the wind speed increment for each step becomes too small. Therefore, this method became so inefficient, and the algorithm is terminated earlier before the limit-point. So, it is necessary to find an alternative method to explore the ultimate winds speeds for long-span aerostatic stability. Figs. 15, 16, and 17 plot the bridge girder deflection shape along a span at selected wind speeds with initial AoA $\alpha_0 = -3°, 0°, 3°$, respectively. Comparing the deflection shape with the simple supported arch beam in Fig. 5, the bridge girder deformation under static wind loads are more concentrated around the middle span. The reason is that the pitch around the middle span increases the aerostatic force along all three directions including drag, lift, and torque, and therefore, the deformation around the middle span is much larger than for an arch beam with constant external force.

The above figures clearly reveal that there are some patterns in the deflection shapes. If the patterns can be extracted as orthogonal mode shapes, it can be used as a series of basic functions ϕ_i in Eq. (4).

Bridge Deflection Mode Shapes Extracted from Singular Value Decomposition

The bridge girder deflection along horizontal direction p, vertical direction h, and rotation θ can compose one deflection vector d_i.

Fig. 12. Wind tunnel test of sectional bridge model.
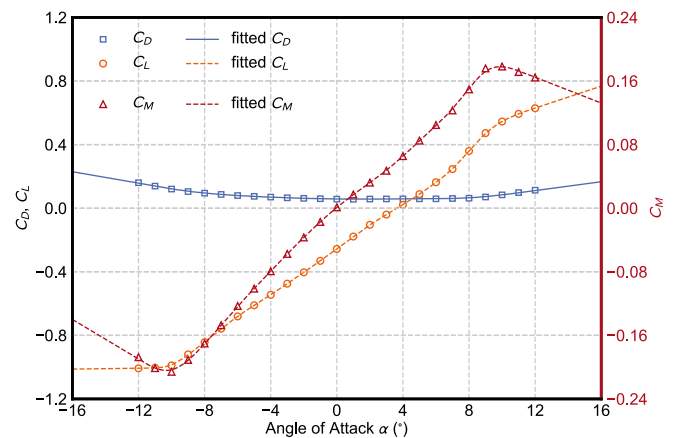

Fig. 13. Aerostatic coefficients of bridge deck.

Next, d_i for different combinations of wind speeds and initial AoA compose the whole deflection matrix $\boldsymbol{D}$.

The typical SVD is performed on $\boldsymbol{D}$, and Fig. 18 plots the first 20 singular values s_i. Fig. 18 clearly reveals that s_1 and s_2 are significantly greater than other singular values. Thus, the order of deformation matrix $\boldsymbol{D}$ can be reduced as $L = 2$, and $\boldsymbol{D}$ can be approximated based on the first two modes as $\boldsymbol{D} \approx \hat{\boldsymbol{\Phi}}\hat{\boldsymbol{\Sigma}}\hat{\boldsymbol{V}}^T$, in which $\hat{\boldsymbol{\Phi}} = [\phi_1, \phi_2]$ and $\hat{\boldsymbol{\Sigma}} = \mathrm{diag}[s_1, s_2]$.
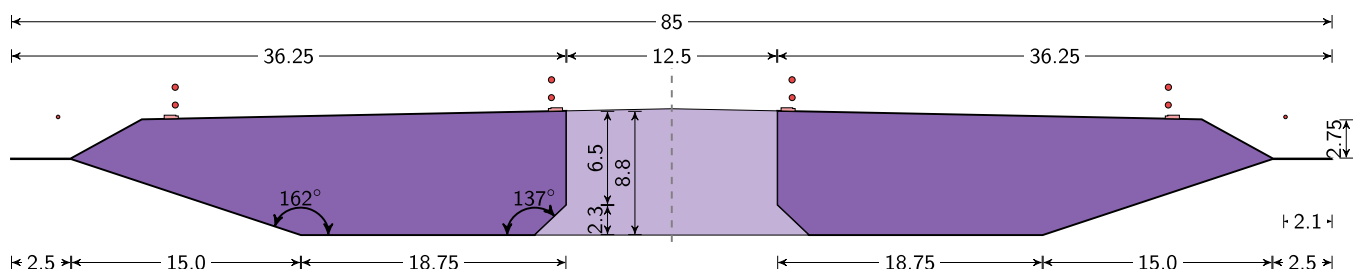

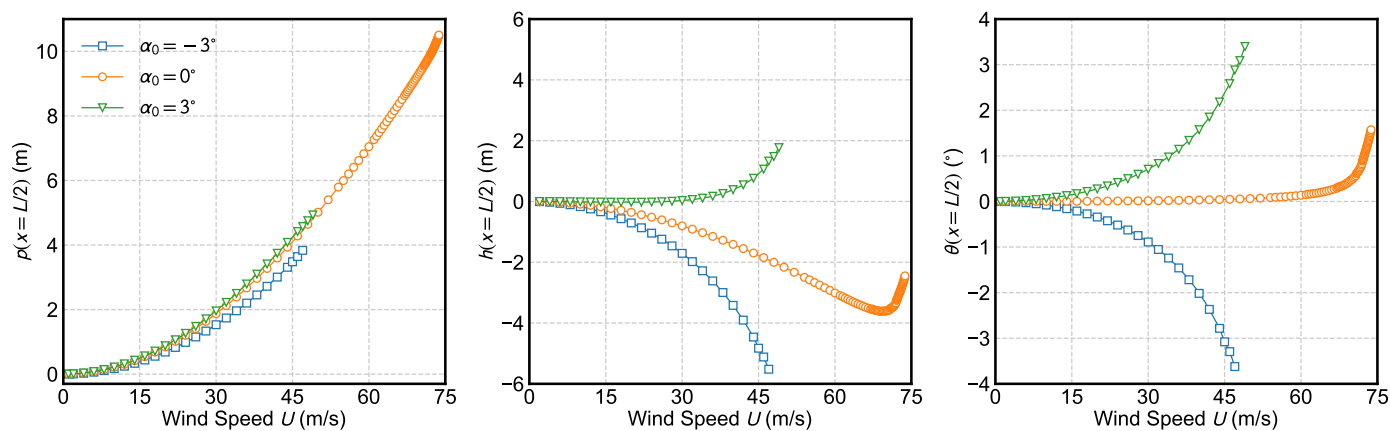**Fig. 11.** Geometries of Xihoumen Bridge section (Unit: cm).

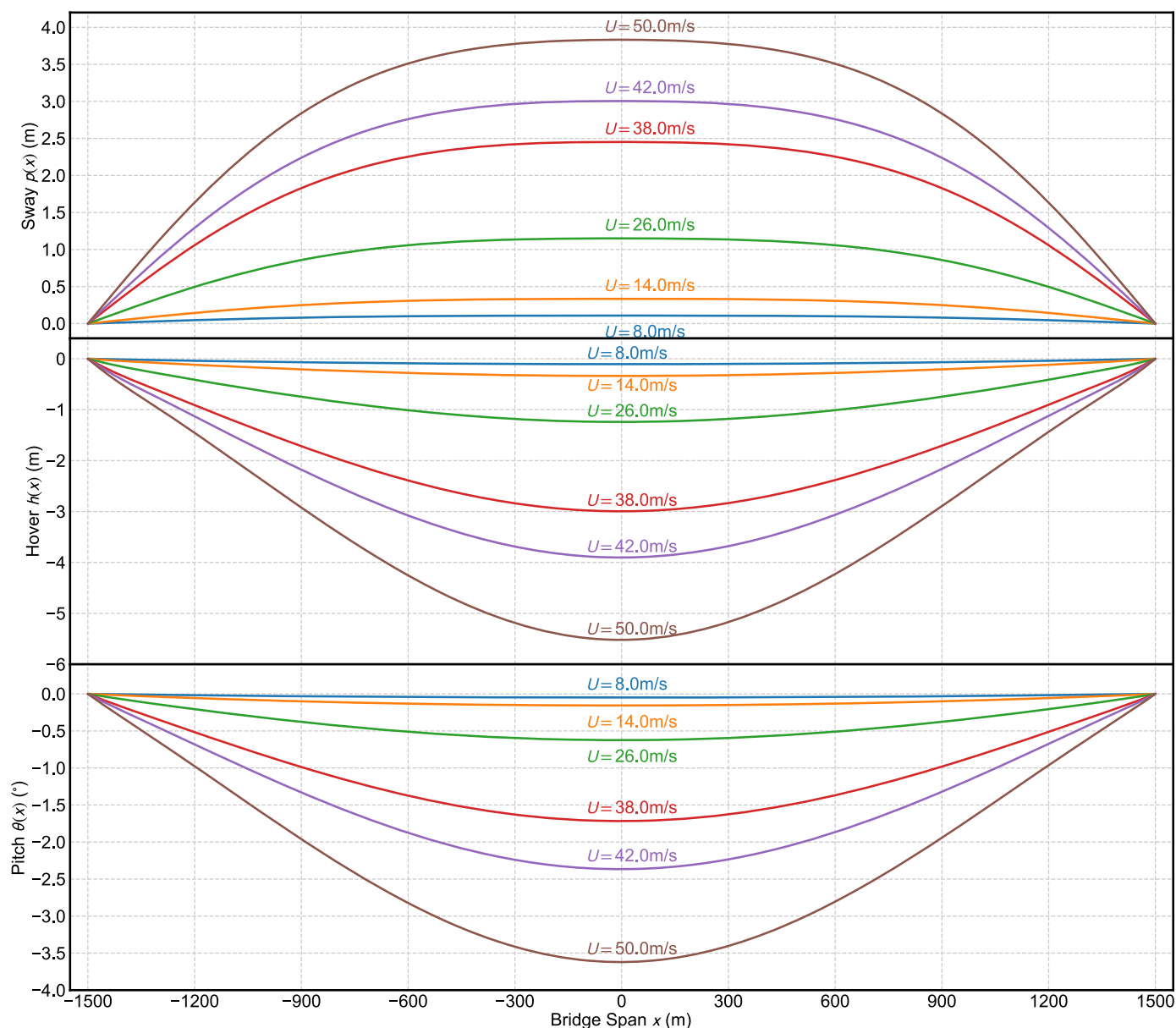**Fig. 14.** The three-directional bridge girder deflection at middle span for various wind speeds and initial AoA.

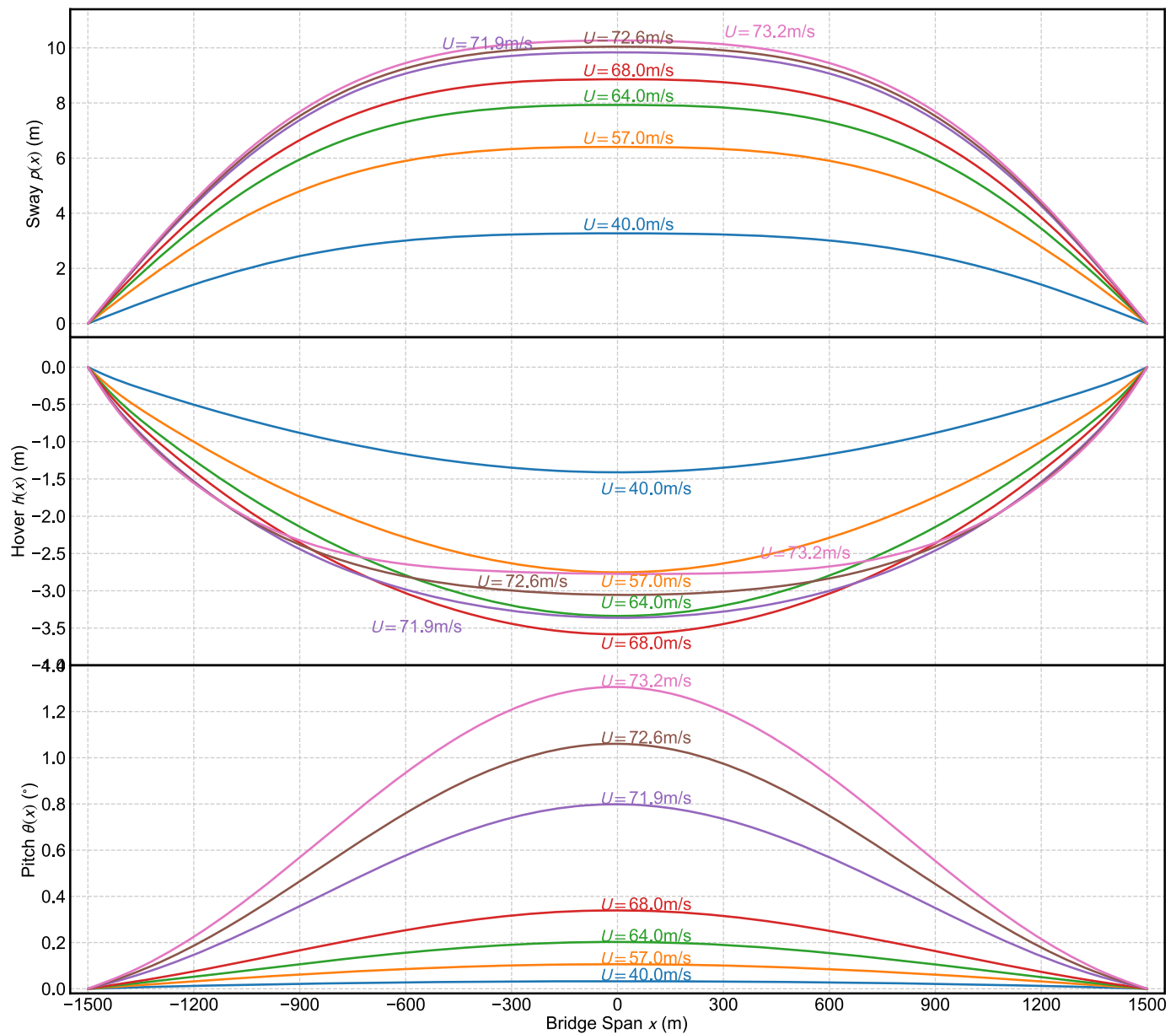**Fig. 15.** The bridge girder three-directional deformation when the initial AoA $\alpha_0 = -3°$.

Fig. 16. The bridge girder three-directional deformation when the initial AoA $\boldsymbol{\alpha}_0 = 0°$.

The associated mode shapes ϕ_1 and ϕ_2 calculated from SVD are plotted in Fig. 19. The major part in ϕ_1 is the sway motion, and the major part in ϕ_2 is the pitch motion. Therefore, a different linear combination of ϕ_1 and ϕ_2 can present the bridge girder deflection under various wind speeds and initial AoA. It should be noted that the mode shape is not only dependent on the structural properties, but also affected by the aerodynamic static coefficients $C_D(\alpha)$, $C_L(\alpha)$, and $C_M(\alpha)$. If either the structural or aerodynamic properties change, the deflection mode shape should be reevaluated.

Determination and Validation of Nonlinear Structural Stiffness Based on ROM

According to the nonlinear ROM coefficients determination methods described in section "Determination of Nonlinear Stiffness Parameters," the coefficients in nonlinear stiffness matrix $\hat{\boldsymbol{K}}$ can be calculated. At first, different generalized bridge girder deflections q_1 in the first mode ϕ_1 are applied on the girder nodes FEM

model built previously. The FEM software can also extract the corresponding reaction forces vector $\boldsymbol{F}$ on the girder nodes. The generalized force for the first node is calculated as $\phi_1^T \boldsymbol{F}$ and, similarly, the second mode generalized force is derived as $\phi_2^T \boldsymbol{F}$.

Fig. 20 plots, when q_1 is in the range of $[-60, 60]$, the generalized forces calculated by FEM in the first mode as $\hat{K}_{11}q_1$ and forces in the second mode as $\hat{K}_{12}q_1$. Similarly, Fig. 21 plots the generalized forces calculated by FEM in the two modes as $\hat{K}_{21}q_2$ and $\hat{K}_{22}q_2$. The nonlinear stiffness matrix in ROM format is determined by fitting the formulas as in Eq. (6), and excellent matches prove that the polynomials in Eq. (6) are able to model the nonlinear stiffness of the bridge girder under aerostatic loads.

In addition to the validation in a single DOF, the validation in coupled two modes ϕ_1 and ϕ_2 is also performed. Figs. 22 and 23 depict the generalized force in the first mode and second mode extracted from FEM software with different combinations of the generalized deformations q_1 and q_2, respectively. The nonlinear stiffness matrix revealed in Eq. (6) is employed to fit the
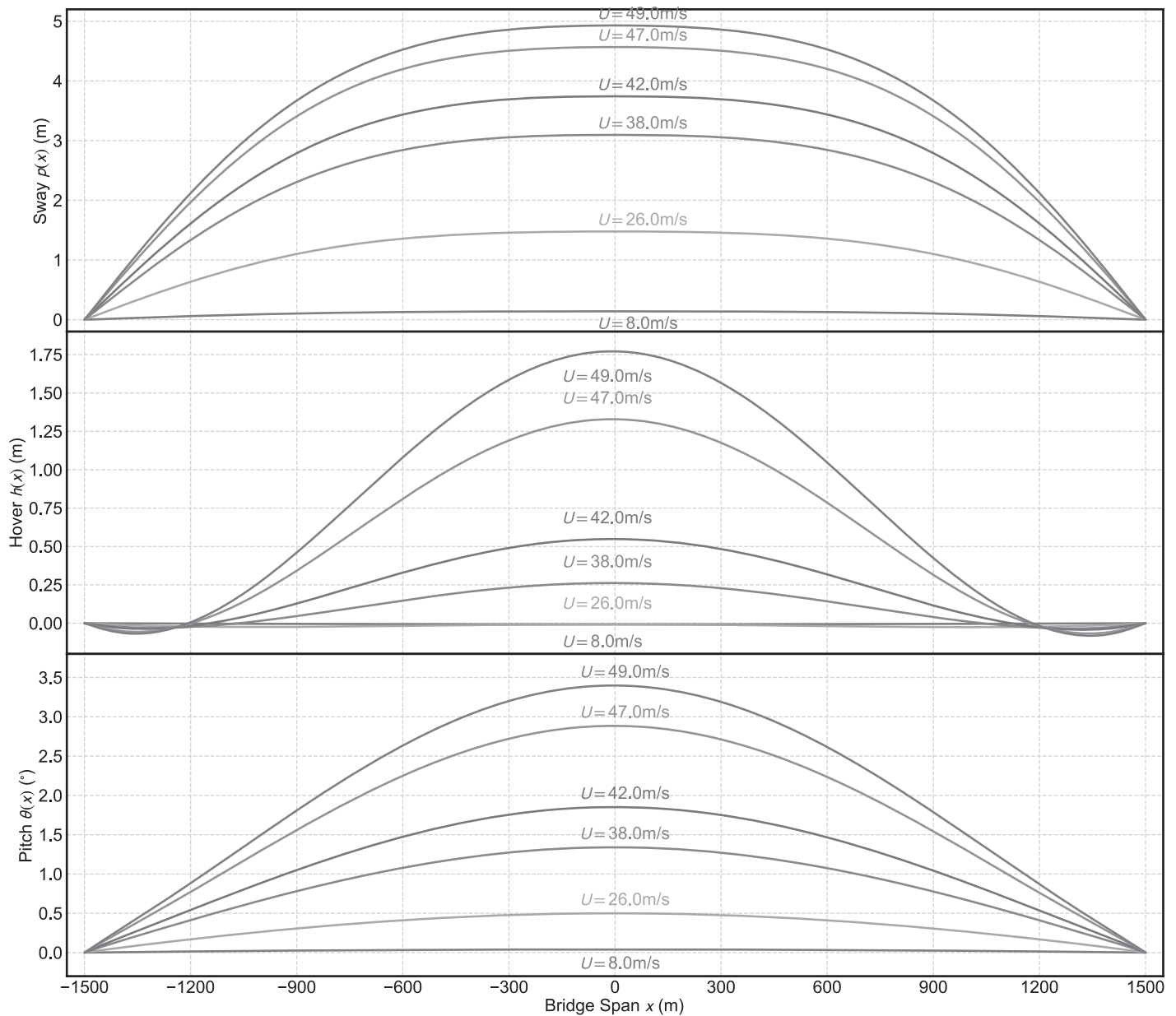
Fig. 17. The bridge girder three-directional deformation when the initial AoA $\alpha_0 = 3°$.

relationship between q_1, q_2 and $\phi_1 F$, $\phi_2 F$, and the FEM results and nonlinear stiffness prove that the coefficients fitted in Eq. (6) can present the aerostatic deformation for this suspension bridge girder.

Validation of Long-Span Bridge Aerostatic Deformation in ROM

After determining the coefficients in the nonlinear stiffness matrix, the bridge girder deformation under the aerostatic loads can be calculated by Eq. (5). Because $L = 2$ in this study, the deformation in ROM is reduced to a roof-find problem for nonlinear equations with an order of 2, when the bridge aerostatic coefficients C_D, C_L, and C_M are predefined. After the generalized deformation, q_1 and q_2, for different wind speeds, are determined by Eq. (5), and the girder deformation along span can be restored using the deformation mode shapes. The middle span three-directional
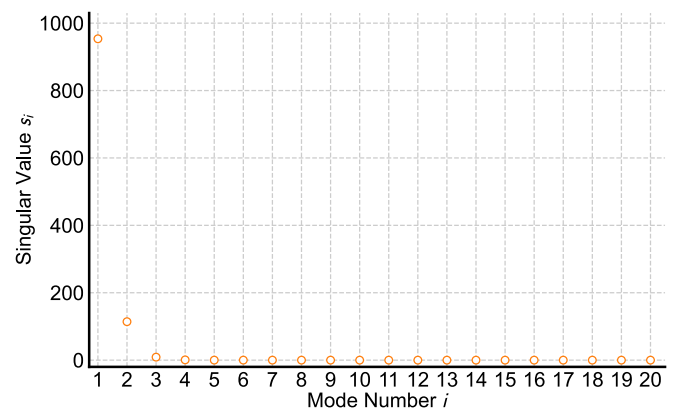

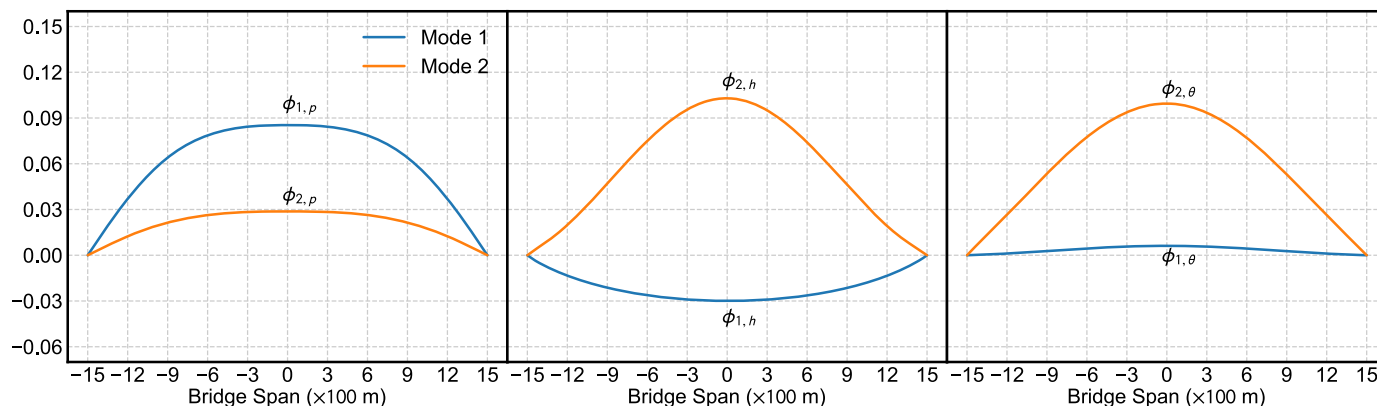**Fig. 18.** The first 20 singular values s_i calculated by SVD on $\mathbf{D}$.

Fig. 19. The first and second mode shapes $\boldsymbol{\phi}_1$ and $\boldsymbol{\phi}_2$ calculated by SVD on $\boldsymbol{D}$.
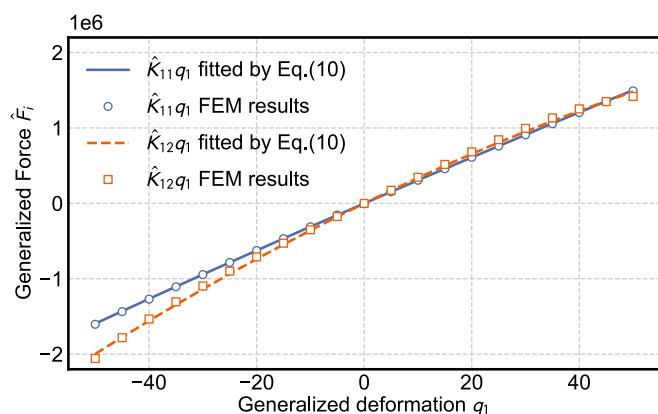

Fig. 20. Generalized force applied on bridge girder for generalized deformation in the first mode $\boldsymbol{q}_1$.
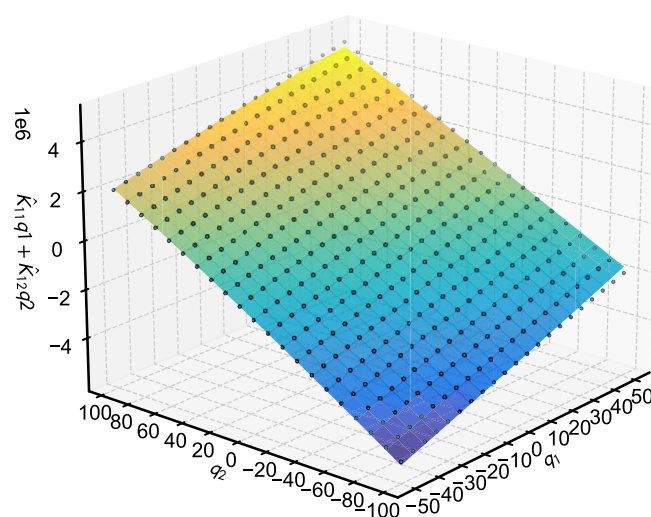
Fig. 22. Generalized force in the first mode $\boldsymbol{\phi}_1$ with different combinations of generalized deformations $\boldsymbol{q}_1$ and $\boldsymbol{q}_2$.
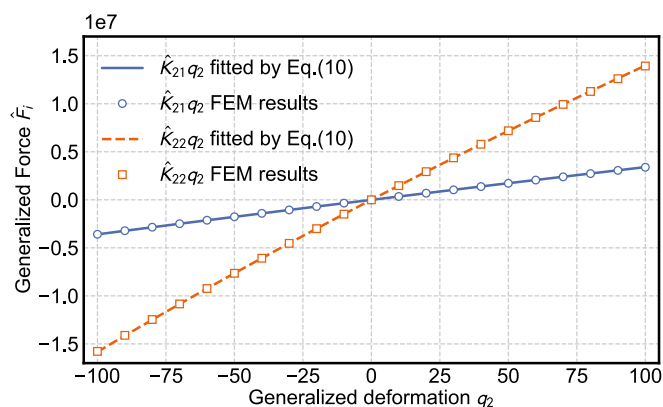

Fig. 21. Generalized force applied on bridge girder for generalized deformation in the second mode $\boldsymbol{q}_2$.
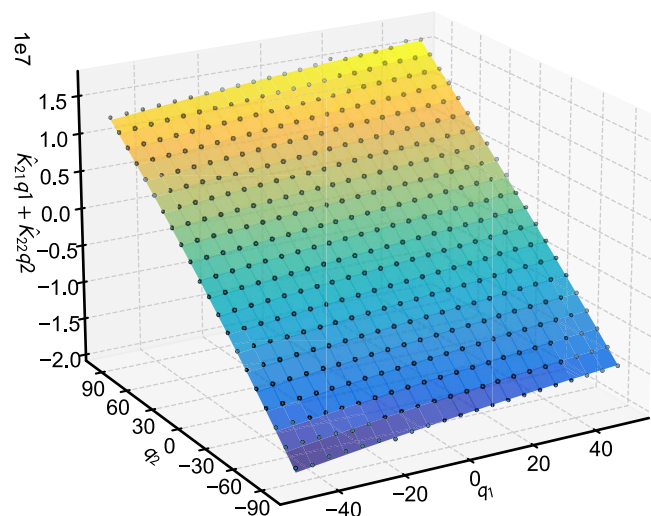
Fig. 23. Generalized force in the second mode $\boldsymbol{\phi}_2$ with different combinations of generalized deformations $\boldsymbol{q}_1$ and $\boldsymbol{q}_2$.

deformations at $x = L/2$ by the ROM method are plotted in Fig. 24 and compared with the results from FEM software. The ROM approximation of a long-span suspension bridge can present the aerostatic deformation under static wind loads as well as the nonlinear FEM stiffness.
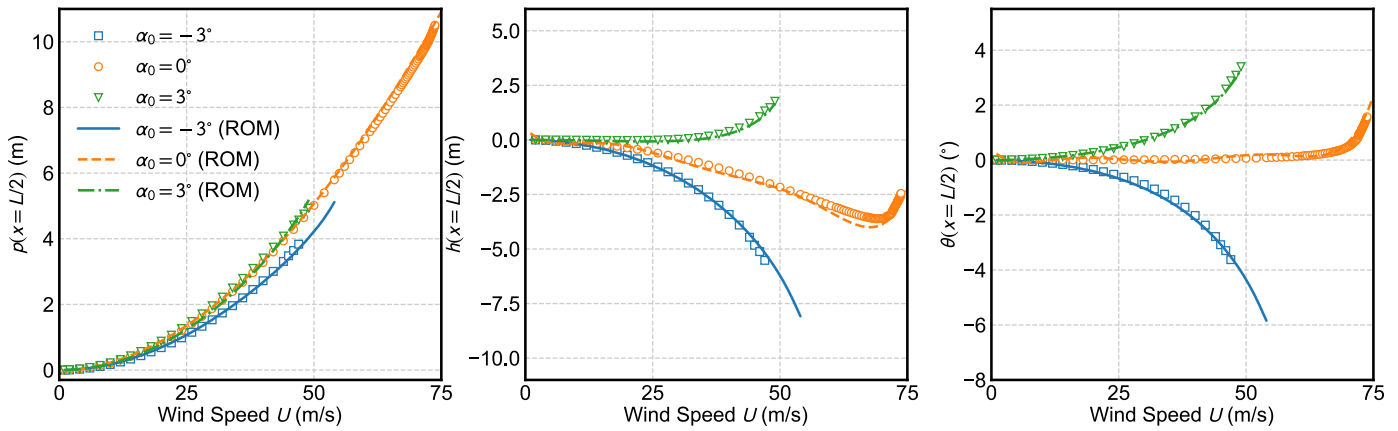
Fig. 24. Comparison of bridge middle span deformations results by ROM and FEM.

Bifurcation of Aerostatic Deformation at High Wind Speeds

By extending the equilibrium path acquired in the last section, the aerostatic bridge deformation at high wind speeds can be obtained in the same ROM methods. Fig. 25 plots the equilibrium path in the generalized coordinates mode 1 and mode 2 for the wind speeds in the range [0–130] m/s. In the range of [0–60] m/s, the deformation is similar to the results depicted in Fig. 24. In the range [60–80] m/s, the structural deformation increases dramatically due to the aerostatic instability caused by the increasing aerostatic loads and decreasing structural stiffness. However, when the wind speed is

Fig. 25. Aerostatic deformation bifurcation with initial AoA $\boldsymbol{\alpha}_0 = 3°$: (a) generalized deformation at first mode $\boldsymbol{q}_1$; and (b) generalized deformation at second mode $\boldsymbol{q}_2$.

beyond 80 m/s, when the bridge deck rotation is over 10°, the aerodynamic loads start to decrease, Therefore, the deformation increasing rate becomes much slower. Also, because of the strong structural nonlinearity, when the wind speed is over 105 m/s, two extra equilibrium paths appear in addition to the first equilibrium path. Thus, a pitchfork bifurcation (Chow and Hale 2012) occurs at this point. It should be noted that this is an imperfection pitchfork bifurcation due the quadratic stiffness terms in Eq. (5).

In addition to the equilibrium path, the stability analysis is performed to examine the stable path and unstable path. The stability criteria are provided in Eqs. (12) and (13). Eq. (12) defines the restoring force when a small perturbation deformation is applied at the equilibrium points. At the equilibrium point for certain wind speed U, $\Delta \boldsymbol{F} = \boldsymbol{0}$. Then the stability of the equilibrium point can be evaluated by Eq. (13), in which $\mathbf{J}(\ )$ is the Jacobian matrix of $\boldsymbol{F}$, and Det[ ] is the matrix determinate operator.

$$\Delta \boldsymbol{F} = \hat{\boldsymbol{K}}\boldsymbol{q} - \boldsymbol{\Phi}^T \boldsymbol{F}(U, \boldsymbol{q}) \tag{12}$$

$$\text{Det}[\ \mathbf{J}(\Delta \boldsymbol{F})] \geq \boldsymbol{0} \tag{13}$$

Det[$\mathbf{J}(\ )$] is normally simply referred to as "the Jacobian," which can be expanded explicitly as Eq. (14)($L = 2$). When the Jacobian of $\Delta \boldsymbol{F}$ is positive, the structure is stable because the restoring force will bring the bridge back to the equilibrium point when small deformation perturbation occurs. However, when the Jacobian of Det[$\mathbf{J}(\Delta \boldsymbol{F})$] is negative, the restoring force cannot stabilize the structure, and any small deformation can disturb the structure from the equilibrium points.

$$\frac{\partial[\Delta \hat{\boldsymbol{K}} q_1 - \phi_1^T \boldsymbol{F}(U, \boldsymbol{q})]}{\partial q_1} + \frac{\partial[\Delta \hat{\boldsymbol{K}} q_2 - \phi_2^T \boldsymbol{F}(U, \boldsymbol{q})]}{\partial q_2}$$
$$- \frac{\partial[\Delta \hat{\boldsymbol{K}} q_1 - \phi_1^T \boldsymbol{F}(U, \boldsymbol{q})]}{\partial q_2} - \frac{\partial[\Delta \hat{\boldsymbol{K}} q_2 - \phi_2^T \boldsymbol{F}(U, \boldsymbol{q})]}{\partial q_1} \geq 0 \tag{14}$$

The stable path and unstable path at different wind speeds are plotted as solid and dashed lines in Fig. 25, respectively. It should be noted that when the wind speed U is in the range of [115–153], there is no stable equilibrium point, and therefore, the "snap-through" (Hrinda 2010) will occur for this bridge if the wind speed exceeds 80 m/s.

Employing the mode shape vectors ϕ_1 and ϕ_2, the bridge three-directional deformation at middle points can also be calculated as in Fig. 26. The bridge girder deformation is observed to increase rapidly after the first critical wind speed at 65 m/s. After the snap-through between 80 and 100 m/s, three deformation paths appear as a bifurcation.
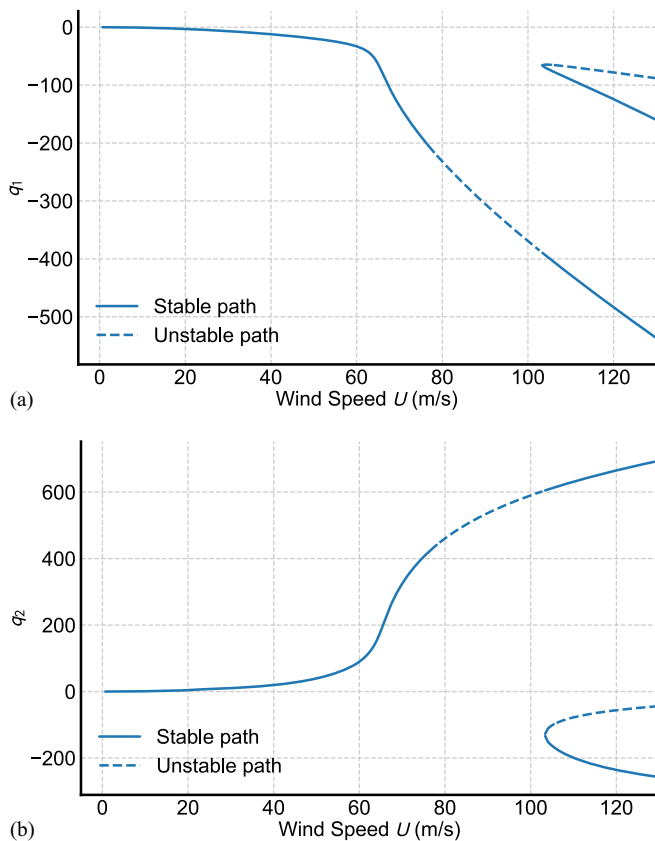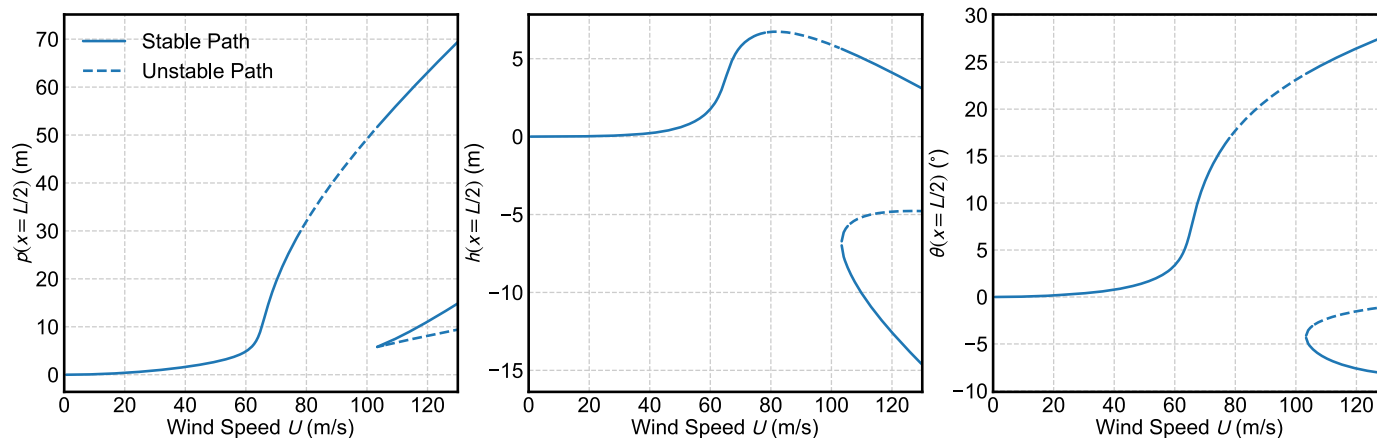
Fig. 26. The multistability of bridge deformation (bifurcation) at high wind speeds.

Conclusions

This study first reviews current methodologies to explore the aerostatic instability of long-span bridges. The two-layer iteration method is able to determine the first buckling point of the long-span bridge under static wind loads considering structural geometry nonlinearity and aerodynamic nonlinearity. However, for the structural behavior after the buckling, the traditional methods based on either the Newton–Raphson or arc-length nonlinear root-finding algorithm cannot completely predict all possible equilibrium paths under large wind speeds. In this study, ROM of aerostatic deformation for long-span bridges is proposed. This method requires an FEM model to be constructed to examine the bridge deformation under various wind speeds and initial AoA. The ensemble of structural deformations calculated from FEM under different wind conditions forms the deformation matrix, on which the SVD is performed to extract the deformation mode shapes. Next, the displacement-based indirect method is employed to determine the ROM nonlinear structural stiffness matrix in the generalized coordinates. Since it is impossible to derive the results of the aerostatic deformation of a large-span bridge under high wind speed from FEM, the accuracy of the method proposed in this study is partially verified by comparing the results of simulating the aerostatic deformation of a bridge under different wind speeds using the static deformation of an arch bridge under different homogeneous loads between the ROM and the FEM. Extending the established ROM to higher wind speeds, two extra equilibrium paths (bifurcation) appear after the structures go through a rapidly increasing range (buckling). After examining the stability along different equilibrium paths, the stable and unstable paths are identified through the Jacobian of structural restoring force under static wind loads.

Data Availability Statement

All data, models, and code generated or used during the study appear in the published article.

Acknowledgments

References

Abbas, T., I. Kavrakov, G. Morgenthal, and T. Lahmer. 2020. "Prediction of aeroelastic response of bridge decks using artificial neural networks." *Comput. Struct.* 231: 106198. https://doi.org/10.1016/j.compstruc.2020.106198.

An, Y., G. Wei, and J. Ou. 2022. "Aerostatic performance improvement based on a novel aerodynamic countermeasure: Simulation and wind tunnel test." *J. Struct. Eng.* 148 (2): 04021254. https://doi.org/10.1061/(ASCE)ST.1943-541X.0003230.

Arena, A., and W. Lacarbonara. 2012. "Nonlinear parametric modeling of suspension bridges under aeroelastic forces: Torsional divergence and flutter." *Nonlinear Dyn.* 70 (4): 2487–2510. https://doi.org/10.1007/s11071-012-0636-3.

Arena, A., W. Lacarbonara, and P. Marzocca. 2016. "Post-critical behavior of suspension bridges under nonlinear aerodynamic loading." *J. Comput. Nonlinear Dyn.* 11 (1): 011005. https://doi.org/10.1115/1.4030040.

Asiedu, L., F. O. Mettle, and E. N. Nortey. 2014. "Recognition of facial expressions using principal component analysis and singular value decomposition." *Int. J. Stat. Syst.* 9 (2): 157–172.

Benjamin Erichson, N., S. L. Brunton, and J. Nathan Kutz. 2017. "Compressed singular value decomposition for image and video processing." In *Proc., IEEE Int. Conf. on Computer Vision Workshops*, 1880–1888. Washington, DC: IEEE Computer Society.

Bergqvist, G., and E. G. Larsson. 2010. "The higher-order singular value decomposition: Theory and an application [lecture notes]." *IEEE Signal Process. Mag.* 27 (3): 151–154. https://doi.org/10.1109/MSP.2010.936030.

Bisplinghoff, R. L., and H. Ashley. 2013. *Principles of aeroelasticity*. 2nd ed. Chelmsford, MA: Courier Corporation.

Boonyapinyo, V., Y. Lauhatanon, and P. Lukkunaprasit. 2006. "Nonlinear aerostatic stability analysis of suspension bridges." *Eng. Struct.* 28 (5): 793–803. https://doi.org/10.1016/j.engstruct.2005.10.008.

Boonyapinyo, V., H. Yamada, and T. Miyata. 1994. "Wind-induced nonlinear lateral-torsional buckling of cable-stayed bridges." *J. Struct. Eng.* 120 (2): 486–506. https://doi.org/10.1061/(ASCE)0733-9445(1994)120:2(486).

Cheng, J., J.-J. Jiang, R.-C. Xiao, and H.-F. Xiang. 2002. "Nonlinear aerostatic stability analysis of Jiang Yin suspension bridge." *Eng. Struct.* 24 (6): 773–781. https://doi.org/10.1016/S0141-0296(02)00006-8.

Chow, S.-N., and J. K. Hale. 2012. Vol. 251 of *Methods of bifurcation theory*. Berlin: Springer Science & Business Media.

Clough, R., and J. Penzien. 1975. *Dynamics of structures*. New York: McGraw-Hill.

Dimentberg, M. 1999. "Nonlinear torsional divergence: Certain exact solutions." *J. Fluids Struct.* 13 (6): 779–784. https://doi.org/10.1006/jfls.1999.0229.

Ding, Y., L. Zhao, R. Xian, G. Liu, H. Xiao, and Y. Ge. 2023. "Aerodynamic stability evolution tendency of suspension bridges with spans from 1,000 to 5,000 m." *Front. Struct. Civ. Eng.* 1: 1–4.

Dunn, P., and J. Dugundji. 1992. "Nonlinear stall flutter and divergence analysis of cantilevered graphite/epoxy wings." *AIAA J.* 30 (1): 153–162. https://doi.org/10.2514/3.10895.

Ebrahimnejad, L., K. Janoyan, D. Valentine, and P. Marzocca. 2014. "Investigation of the aerodynamic analysis of super long–span bridges by using era-based reduced-order models." *J. Bridge Eng.* 19 (9): 04014033. https://doi.org/10.1061/(ASCE)BE.1943-5592.0000607.

Fazelzadeh, S. A., and A. Mazidi. 2011. "Nonlinear aeroelastic analysis of bending-torsion wings subjected to a transverse follower force." *J. Comput. Nonlinear Dyn.* 6 (3): 031016. https://doi.org/10.1115/1.4003288.

Ge, Y., J. Xia, L. Zhao, and S. Zhao. 2018. "Full aeroelastic model testing for examining wind-induced vibration of a 5,000 m spanned suspension bridge." *Front. Built Environ.* 4: 20. https://doi.org/10.3389/fbuil.2018.00020.

Hirai, A., I. Okauchi, M. Ito, and T. Miyata. 1967. "Studies on the critical wind velocity for suspension bridges." In *Proc., Int. Research Seminar on Wind Effects on Buildings and Structures*, 81–103. Toronto, ON: Univ. of Toronto Press.

Hollkamp, J. J., R. W. Gordon, and S. M. Spottswood. 2005. "Nonlinear modal models for sonic fatigue response prediction: A comparison of methods." *J. Sound Vib.* 284 (3–5): 1145–1163. https://doi.org/10.1016/j.jsv.2004.08.036.

Hrinda, G. 2010. "Snap-through instability patterns in truss structures." In *Proc., 51st AIAA/ASME/ASCE/AHS/ASC Structures, Structural Dynamics, and Materials Conf. 18th AIAA/ASME/AHS Adaptive Structures Conf. 12th*, 2611. Reston, VA: American Institute of Aeronautics and Astronautics (AIAA).

Hu, C., Z. Zhou, and B. Jiang. 2019. "Effects of types of bridge decks on competitive relationships between aerostatic and flutter stability for a super long cable-stayed bridge." *Wind Struct.* 28 (4): 255–270.

Kielhöfer, H. 2011. Vol. 156. *Bifurcation theory: An introduction with applications to partial differential equations*. Berlin: Springer Science & Business Media.

Kim, B., and K. T. Tse. 2018. "Pod analysis of aerodynamic correlations and wind-induced responses of two tall linked buildings." *Eng. Struct.* 176: 369–384. https://doi.org/10.1016/j.engstruct.2018.09.013.

Klema, V., and A. Laub. 1980. "The singular value decomposition: Its computation and some applications." *IEEE Trans. Autom. Control* 25 (2): 164–176. https://doi.org/10.1109/TAC.1980.1102314.

Ko, J., S. Xue, and Y. Xu. 1998. "Modal analysis of suspension bridge deck units in erection stage." *Eng. Struct.* 20 (12): 1102–1112. https://doi.org/10.1016/S0141-0296(97)00207-1.

Koenker, R., P. Ng, and S. Portnoy. 1994. "Quantile smoothing splines." *Biometrika* 81 (4): 673–680. https://doi.org/10.1093/biomet/81.4.673.

Leahu-Aluas, I., and F. Abed-Meraim. 2011. "A proposed set of popular limit-point buckling benchmark problems." *Struct. Eng. Mech.* 38 (6): 767–802. https://doi.org/10.12989/sem.2011.38.6.767.

Lorente, L., J. Vega, and A. Velazquez. 2008. "Generation of aerodynamics databases using high-order singular value decomposition." *J. Aircr.* 45 (5): 1779–1788. https://doi.org/10.2514/1.35258.

Mignolet, M. P., A. Przekop, S. A. Rizzi, and S. M. Spottswood. 2013. "A review of indirect/non-intrusive reduced order modeling of nonlinear geometric structures." *J. Sound Vib.* 332 (10): 2437–2460. https://doi.org/10.1016/j.jsv.2012.10.017.

Ministry of Transports of the People's Republic of China. 2018. Wind-resistant design specification for highway bridges. JTG/T 3360-01-2018. Beijing: Ministry of Transports of the People's Republic of China.

Montoya, M. C., S. Hernández, A. Kareem, and F. Nieto. 2021. "Efficient modal-based method for analyzing nonlinear aerostatic stability of long-span bridges." *Eng. Struct.* 244: 112556. https://doi.org/10.1016/j.engstruct.2021.112556.

Muller, N., L. Magaia, and B. M. Herbst. 2004. "Singular value decomposition, eigenfaces, and 3D reconstructions." *SIAM Rev.* 46 (3): 518–545. https://doi.org/10.1137/S0036144501387517.

Muravyov, A. A., and S. A. Rizzi. 2003. "Determination of nonlinear stiffness with application to random vibration of geometrically nonlinear structures." *Comput. Struct.* 81 (15): 1513–1523. https://doi.org/10.1016/S0045-7949(03)00145-7.

Przekop, A., M. S. Azzouz, X. Guo, C. Mei, and L. Azrar. 2004. "Finite element multiple-mode approach to nonlinear free vibrations of shallow shells." *AIAA J.* 42 (11): 2373–2381. https://doi.org/10.2514/1.483.

Rufai, A. M., G. Anbarjafari, and H. Demirel. 2014. "Lossy image compression using singular value decomposition and wavelet difference reduction." *Digital Signal Process.* 24: 117–123. https://doi.org/10.1016/j.dsp.2013.09.008.

Shao, Y. 2010. "Refinements on aerodynamic and aerostatic stability of super long span suspension bridges with box girder." Ph.D. dissertation, Dept. of Bridge Engineering, Tongji Univ.

Simiu, E., and R. H. Scanlan. 1996. *Wind effects on structures: Fundamentals and applications to design*. 3rd ed. Hoboken, NJ: John Wiley & Sons.

Simiu, E., and D. Yeo. 2019. *Wind effects on structures: Modern structural design for wind*. 4th ed. Hoboken, NJ: Wiley–Blackwell.

Tamura, Y., H. Ueda, H. Kikuchi, K. Hibi, S. Suganuma, and B. Bienkiewicz. 1997. "Proper orthogonal decomposition study of approach wind-building pressure correlation." *J. Wind Eng. Ind. Aerodyn.* 72: 421–431. https://doi.org/10.1016/S0167-6105(97)00270-5.

Tsay, J.-Y. 2021. "Feasibility study of super-long span bridges considering aerostatic instability by a two-stage geometric nonlinear analysis." *Int. J. Struct. Stab. Dyn.* 21 (03): 2150033. https://doi.org/10.1142/S0219455421500334.

Yang, Y., R. Zhou, Y. Ge, D. Mohotti, and P. Mendis. 2015. "Aerodynamic instability performance of twin box girders for long-span bridges." *J. Wind Eng. Ind. Aerodyn.* 145: 196–208. https://doi.org/10.1016/j.jweia.2015.06.014.

Zamiri, G., and S.-R. Sabbagh-Yazdi. 2021. "Pseudo-3D aerostatic instability analysis of suspension bridge deck using finite volume solution of wind flow and element-free galerkin of structure." In Vol. 31 of *Structures*, 500–512. Amsterdam, Netherlands: Elsevier.

Zhang, Z., Y. Ge, and Z. Chen. 2015. "On the aerostatic divergence of suspension bridges: A cable-length-based criterion for the stiffness degradation." *J. Fluids Struct.* 52: 118–129. https://doi.org/10.1016/j.jfluidstructs.2014.10.005.

Zhang, Z., and L. Zhu. 2021. "Wind-induced symmetric and asymmetric static torsional divergence of flexible suspension bridges." *J. Fluids Struct.* 103: 103263. https://doi.org/10.1016/j.jfluidstructs.2021.103263.